International Journal of Impact Engineering 36 (2009) 720–728

Contents lists available at ScienceDirect

International Journal of Impact Engineering

journal homepage: www.elsevier.com/locate/ijimpeng

# Jet engine fan blade containment using an alternate geometry

K.S. Carney [a,*], J.M. Pereira [a], D.M. Revilock [a], P. Matheny [b]

[a] *NASA Glenn Research Center, 21000 Brookpark Road, Cleveland, OH 44135, USA*
[b] *Florida Turbine Technology, West Palm Beach, FL, USA*

A R T I C L E  I N F O

*Article history:*
Received 5 November 2007
Received in revised form
8 August 2008
Accepted 3 October 2008
Available online 1 November 2008

*Keywords:*
Containment
Fan case
Blade off
Turbine engine
Very high strain rate material behavior

A B S T R A C T

With a goal of reducing jet engine weight, simulations of a fan blade containment system with an alternate geometry were tested and analyzed. A projectile simulating a fan blade was shot at two alternate geometry containment case configurations using a gas gun. The first configuration was a flat plate representing a standard case configuration. The second configuration was a flat plate with a radially convex curve section at the impact point. The curved surface was designed to force the blade to deform plastically, dissipating energy before the full impact of the blade is received by the plate. The curved case was able to tolerate a higher impact velocity before failure. The computational model was developed and correlated with the tests and a weight savings assessment was performed. For the particular test configuration used in this study the ballistic impact velocity of the curved plate was approximately 60 m/s (200 ft/s) greater than that of the flat plate. For the computational model to successfully duplicate the test, the very high strain rate behavior of the materials had to be incorporated.

Published by Elsevier Ltd.

## 1. Introduction

In order to insure passenger and crew safety, international aviation regulatory bodies, such as the Federal Aviation Administration in the United States and the Joint Aviation Authorities in Europe require that in commercial jet engines a system must exist which will not allow any compressor or turbine blade to perforate the engine case in the event that it is released from a disk during engine operation [1]. Due to this requirement the fan case is the heaviest single component of a jet engine. The Federal Aviation Administration further requires that jet engine manufacturers demonstrate, through a certification test, that the most critical blade be contained within the engine when a blade is released while the engine is running at full rated thrust [2]. The most critical blade in the engine, in terms of maximum kinetic energy, is invariably the fan blade, and the system designed to prevent it from penetrating the engine is called the fan containment system.

The fan containment system includes a cylindrical case which surrounds the fan blades and disk. In modern high bypass turbine engines the fan blades are large and due to the large diameter of the fan section of the engine, the fan cases contribute significantly to overall engine weight. There are two general types of fan containment systems, commonly referred to as hardwall and softwall systems. Hardwall systems consist of a relatively stiff section of the engine case that has sufficient strength to prevent perforation if impacted by a blade. Softwall systems usually consist of a relatively thin inner ring, surrounded by layers of dry fabric. Both systems include ribs and stiffeners which enhance system stiffness and both typically have generally flat cylindrical geometries. The geometry of the fan case can affect containment response. A careful selection of the geometry can improve containment and efficiency, allowing for case thickness reduction and reduced engine weight.

The loss of blades in turbine engines, such as those shown in Fig. 1, can be initiated by material failure due to fatigue, a bird strike [3], or some other foreign object damage. The fan blades are initially rotating at a very high rate, on the order of 5000 rpm. A released blade will attempt to follow a tangential trajectory, rotating about its center of gravity. That trajectory will cause the blade to impact the containment case at a relatively consistent angle and orientation. The character of a blade off impact, including point of impact, is surprisingly repeatable for an event which is triggered randomly. As a result, the blade off event may be tested and designed for in a deterministic manner.

Future fan cases may incorporate an alternate geometry with a shallow convex curve in the radial direction of the cylindrical case as depicted in Fig. 2. As a released blade strikes the convex curve it will deform, dissipating its kinetic energy in plastic deformation before the full weight of the blade impacts. The proposal that the radially convex curved geometry will aid in containment was preliminarily explored using LS-DYNA [4] analysis. After showing promise in the preliminary analysis, ballistic tests on scaled, representative flat plates were performed to evaluate the concept. A final analysis was correlated with these tests, giving an estimate

---

* Corresponding author. Tel.: +1 216 433 2386.
*E-mail address:* kelly.s.carney@nasa.gov (K.S. Carney).

0734-743X/$ – see front matter Published by Elsevier Ltd.
doi:10.1016/j.ijimpeng.2008.10.002

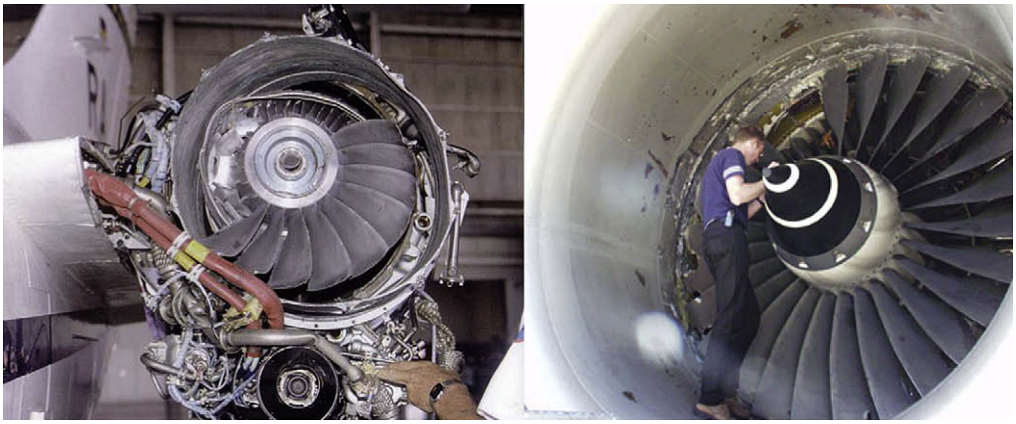

**Fig. 1.** Fan blade losses in two different size engines.

of the potential weight savings and yielding insight into the behavior of the subject materials at very high strain rates. The incorporation of the material behavior at very high strain rates was found necessary to achieve accurate results. This paper discusses the ballistic testing, very high strain rate behavior of metals and the analysis, and demonstrates that a radially convex curved geometry shows promise.

## 2. Ballistic impact testing

Ballistic impact testing was conducted at the NASA Glenn Research Center Ballistic Impact Laboratory using a single stage compressed gas gun. The gun consisted of a pressure vessel with a volume of 0.35 $m^3$ (12.5 $ft^3$), a gun barrel with a length of 12.2 m (40 ft) and an inner diameter of 20.32 cm (8.00 in) (Fig. 3). The pressure vessel and the gun barrel are mated by a burst valve consisting of a number of layers of Mylar® sheet. Helium gas is used as the propellant. The pressurized helium is released into the gun barrel by applying a voltage across a Nichrome wire embedded in the Mylar sheets, causing the Mylar sheets to rupture. The velocity of the projectile is controlled by the gas pressure.

For this test program the projectile was supported by a wood block inside a cylindrical aluminum sabot that fit snugly inside the gun barrel. The sabot was stopped at the end of the gun barrel by a thick steel plate with a rectangular slot large enough to allow the projectile to pass through. The gun barrel was evacuated to reduce blast loading on the specimen and to reduce the amount of pressure needed to achieve the desired impact velocity.

For the test targets, the fan case was represented by 0.6096 m by 0.6096 m (24.0/24.0 in) in 304L stainless steel plates, with a thickness of 0.47625 cm (3/16 in). Half of the plates were flat and half had a shallow convex curve with a height of 0.79375 cm (5/6 in) and a width of 12.7 cm (5.0 in), as shown in Fig. 4. The plates were securely clamped at their edges and two simple supports were placed on either side of the target, 0.2032 m (8.0 in) apart. The blades were simulated by a projectile made from Ti–6Al–4V titanium which nominally weighed 468.26 gm (1.0323 lbs). The blade simulating projectile was 12.7 cm (5.0 in) long, 9.652 cm (3.8 in) wide, and 0.508 cm (0.2 in) thick at the narrow end, and 1.27 cm (0.5 in) thick at the thick end, as shown in Fig. 5. The plates were held at 45° in relation to the trajectory of the blade. The blade orientation was in relation to its trajectory, opposite to that of the plate, as shown in Fig. 6.

High speed digital video cameras (Phantom 5, Vision Research, Wayne, NJ) were used to record the position, orientation and velocity of the projectile during the experiment. The recording speed was 11,200 frames per second, with a 256 × 256 pixel resolution. One camera was located at the side of the impact point and the other was at an oblique angle. For each test the position of the projectile was recorded as a function of time. The impact velocity was determined by fitting a straight line to the position time history

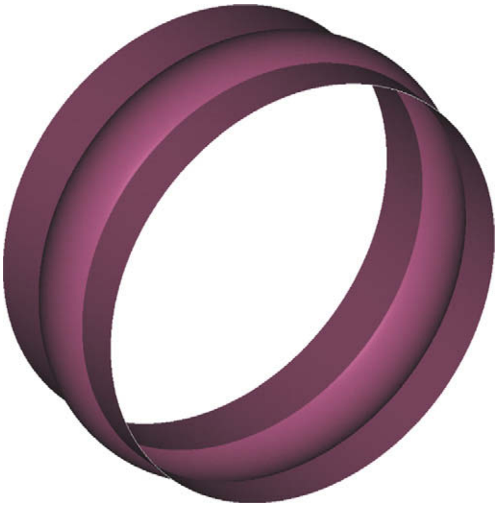

**Fig. 2.** A fan containment case with a radially convex curve in its geometry.

**Fig. 3.** The NASA Glenn Research Center Ballistic Impact Laboratory gas gun.

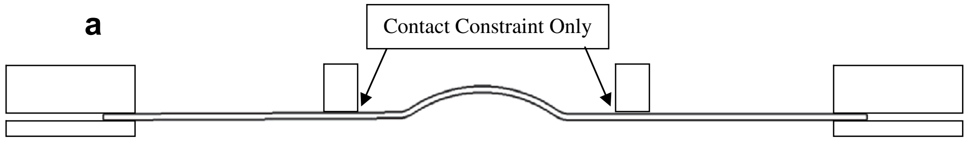

Schematic of Test Boundary Conditions

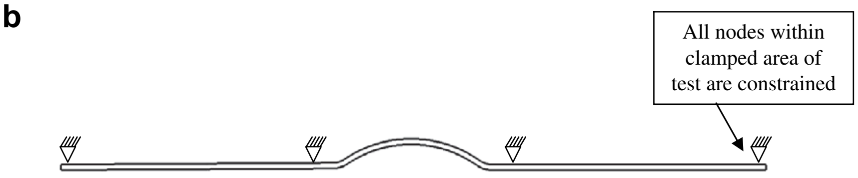

Schematic of Analytical Boundary Conditions

**Fig. 4.** The 304L stainless steel target plate in a view which shows the convex curve geometry.

while in free flight and averaging the slopes of the resulting lines. In general, the projectile was obscured by the specimen during the impact itself, so it was not possible to obtain accurate enough position data to calculate the projectile deceleration and the resulting force on the projectile during the impact. After each test the plastic deformation and failure of both the target and the projectile were evaluated.

## 3. Analysis

### 3.1. Material modeling

The finite element analysis was conducted using LS-DYNA [4,5], a commercially available explicit dynamic analysis code. The material model of the Titanium was defined using the parameters defined above and the LS-DYNA Piecewise Linear Plasticity material model, Mat 24. The material model of the Stainless Steel was defined using the parameters defined above and the LS-DYNA Plasticity With Damage material mode, Mat 81. The finite element discretization of the target plate consisted of 57,600 equally sized shell elements using the Belytschko–Tsay formulation. The dimensions of the shell elements were approximately 0.254 cm by 0.254 cm (0.1/0.1 in). The outside edges of the plates were clamp constrained and 0.2032 m (8.0 in) wide simple supports, on either side of the impact area, were constrained only in the direction of impact. The blade was modeled with 6080 constant stress solid elements. The dimensions of the solid elements were approximately 0.254 cm by 0.254 cm by 0.254 cm (0.1/0.1/0.1 in).

Both the 304L stainless steel and Ti–6Al–4V titanium were modeled using plasticity models [4,6] where the stress–strain behavior is directly defined as follows,

$$\frac{1}{2}s_{ij}s_{ij} \cong \frac{\sigma_y^2}{3}, \tag{1}$$

where $s_{ij}$ is the deviatoric stress component,

$$\sigma_y = \widehat{\beta}\left[\sigma_0 + \widehat{f}_h\left(\varepsilon^p_{eff}\right)\right], \tag{2}$$

$\widehat{\beta}$ is the strain rate scale factor, $\widehat{f}_h(\varepsilon^p_{eff})$ is the hardening function, with the carets denoting that they are tabular defined functions, and $\varepsilon^p_{eff}$ is the effective plastic strain. The Ti–6Al–4V titanium blade material model was defined using the material property data shown in Table 1 and by directly defining several stress–strain curves in tabular form where each curve defines the response at a specific strain rate. Failure was defined at 0.22 effective plastic strain. The strain rate sensitivities for the high and very high strain rates were obtained from Nicholas [7], Lesuer [8], and Wulf [9].

The material model for the 304L stainless steel plates also included damage [4,6], where the stress is scaled by $1/1-\omega$, and where

$$\omega = \frac{\varepsilon^p_{eff} - \varepsilon^p_{fail}}{\varepsilon^p_{rupture} - \varepsilon^p_{fail}} \quad \text{if} \quad \varepsilon^p_{fail} \le \varepsilon^p_{eff} \le \varepsilon^p_{rupture}. \tag{3}$$

This damage model successfully reproduces the tearing of steel which was observed in the ballistic tests. The material behavior of 304L was specified using the material property data shown in Table 2 and by directly defining several stress–strain curves in tabular form where each curve defines the response at a specific strain rate. The onset of damage was defined as 0.36 effective plastic strain, with element erosion occurring at 0.56 plastic strain. Tension tests were conducted to determine the static stress–strain curve, and the value of the onset of damage. The high strain rate

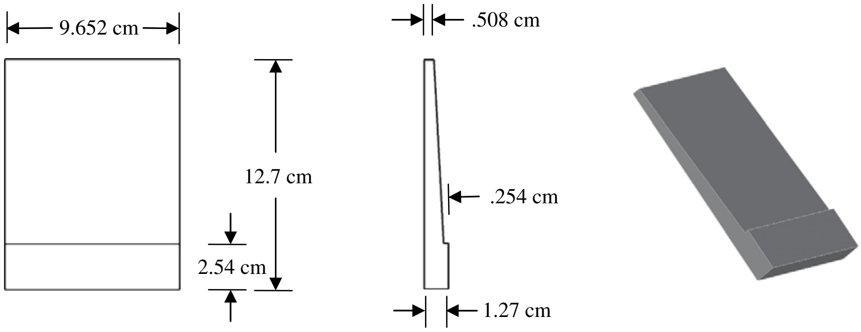

**Fig. 5.** The blade simulating projectile, which is made of Ti–6Al–4V titanium.

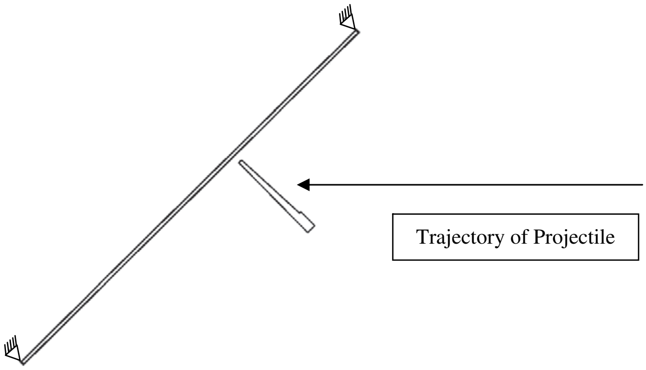

**Fig. 6.** The orientation of the blade simulating projectile as it impacts the plate.

data used to create this model was obtained from Nicholas [7], and for very high strain rates, the strain rate sensitivity was derived from Dowling [10].

The behavior of both the titanium and the stainless steel at strain rates greater than $5 \times 10^3\ s^{-1}$ was an important factor in defining the dynamic and failure response of the complete system. Including the dramatic increase in strain rate sensitivity at strain rates greater than $5 \times 10^3\ s^{-1}$ of both the 304L stainless steel and Ti–6Al–4V titanium was critical in obtaining a representative analysis. The very high strain rate sensitivities of both the stainless steel [10] and the titanium [9] were used to extrapolate the strain rate curves beyond the tested strain rates. Fig. 7 shows the strain rate sensitivities used in the analysis.

### 3.2. *Very high strain rate material behavior*

As stated in the previous section, a critical aspect in obtaining a representative analysis was to include the material behavior at very high strain rates of greater than $10^5\ s^{-1}$. This is a region where it is difficult to measure the properties experimentally, and there is some debate concerning the physical nature of the assumed material behavior. Since including this behavior is critical to accurate modeling, and there is some uncertainty introduced by using the published data as is, a more detailed review of that literature is warranted. In addition, as this published test data is limited, and there is disagreement in it as to the real nature of the general behavior of metals at strain rates of $10^4\ s^{-1}$ and greater, a review of the literature of alloys other than 304L stainless steel and Ti–6Al–4V titanium is also justified.

The tensile behavior, including full stress–strain curves, of 21 different metals and alloys under low to high strain rates is given by Nicholas [7]. These include the two materials of interest in the present work, 304L stainless steel and Ti–6Al–4V titanium. The tests were conducted using a split-Hopkinson pressure bar, described by Gray [11]. The maximum strain rate achieved in these tests is approximately $10^3\ s^{-1}$.

Campbell and Ferguson [12] found that the shear strength of a mild steel, En 3B, is dependent on strain rate as follows: low strain rate, region I being characterized by a small, nearly constant increase in strength with the logarithm of shear strain rate; region II where the increase is still constant with the logarithm of the strain rate, but the rate dependence is considerably higher; and region IV, corresponding to strain rates of greater than $5 \times 10^3\ s^{-1}$ where the increase in shear strength is directly proportional to the strain rate. Fig. 8, showing these regions, is reprinted from Ref. [12]. The authors identify region I as being dominated by long-range internal stresses due to dislocations, precipitate particles, and grain boundaries. Region II is identified as being controlled by the thermal activation of dislocation motion, and region IV being governed by short-range barriers in combination with an additional dissipative mechanism, but failure not a function of temperature. It is also shown that almost identical strain rate sensitivity behavior for room temperature steel is obtained from dynamic punching, using data from Dowling and Harding [13], and tension, using data from Campbell and Cooper [14], as that from shear loading.

**Table 1**
Material model properties of Ti–6Al–4V titanium.

| | | |
|---|---|---|
| $\rho$ | Density | 4650.22 kg/m$^3$ (0.168 lbs/in$^3$) |
| $E$ | Young's modulus | 110.316 GPa (16.0 × 10$^6$ lbs/in$^2$) |
| $\nu$ | Poisson's ratio | 0.31 |
| $\sigma_y$ | Yield stress | 1.00663 GPa (1.46 × 10$^5$ lbs/in$^2$) |
| $E_T$ | Tangent modulus | 1.59269 GPa (2.31 × 10$^5$ lbs/in$^2$) |
| $\varepsilon^p_{fail}$ | Plastic strain to failure | 0.22 |

**Table 2**
Material model properties of 304L stainless steel.

| | | |
|---|---|---|
| $\rho$ | Density | 7750.373 kg/m$^3$ (0.280 lbs/in$^3$) |
| $E$ | Young's modulus | 193.053 GPa (28.0 × 10$^6$ lbs/in$^2$) |
| $\nu$ | Poisson's ratio | 0.305 |
| $\sigma_y$ | Yield stress | 339.222 MPa (4.92 × 10$^4$ lbs/in$^2$) |
| $E_T$ | Tangent modulus[a] | ~165 MPa (~2.4 × 10$^5$ lbs/in$^2$) |
| $\varepsilon^p_{fail}$ | Plastic strain to failure | 0.36 |

[a] Approximate value. Plastic behavior defined by tabular stress–strain curve.

Dowling, Harding, and Campbell extended the work on mild steel in Ref. [10] to aluminum, copper, and brass in Ref. [13]. The dynamic punch loading of all four of these materials showed the same general strain rate sensitivity as the mild steel in shear of Ref. [12]. For all four of these materials, at room temperature, there was a small increase in strength, proportional to the logarithm of strain rate, at rates below $10^{-1}\ s^{-1}$, greater increase in sensitivity at rates between $10^{-1}\ s^{-1}$ and $10^3\ s^{-1}$, and at rates above $10^3\ s^{-1}$ even greater sensitivity with the increase being proportional to the strain rate. While the general behavior of the four metals is shown to be similar, the strain rate sensitivity of the four metals is not identical.

Lesuer [8], compiled the stress–strain rate response of Ti–6Al–4V titanium alloy from the available literature, and included some additional test data. Very high strain rate data at rates greater than $10^3\ s^{-1}$ was included from Wulf [9] and Meyer [15]. This data shows titanium exhibiting the same shift documented by Dowling et al., [13] for the other metals. When strain rates exceed approximately $5 \times 10^3\ s^{-1}$, the strain rate sensitivity becomes a function of the strain rate, while at strain rates lower than this it is a function of the

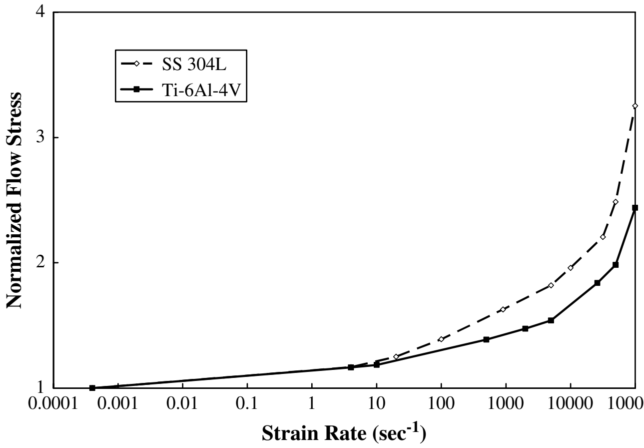

**Fig. 7.** The strain rate sensitivity of Ti–6Al–4V and SS-304L utilized in the analytical model.

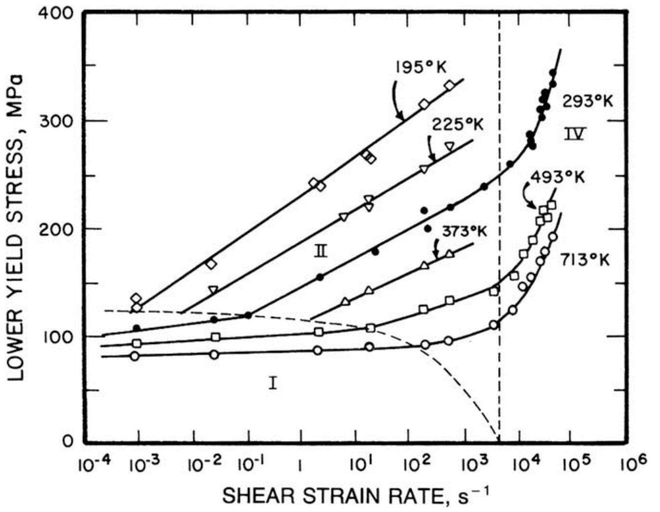

**Fig. 8.** Variation of lower yield stress with strain rate, at constant temperature. From Ref. [12].

logarithm of the strain rate. Fig. 9 is taken from Ref. [8], showing this behavior. Wulf [9] also shows that the strain rate sensitivity is not constant.

Frost and Ashby [16] present a strain–rate map for titanium which shows the mechanisms responsible for the various failure behaviors. This map associates room temperature failure in regions I and II with obstacle controlled plasticity, and failure in region IV with adiabatic shear. In addition it identifies a region of drag-controlled plasticity failure at strain rates on the order of $10^5\ s^{-1}$ and shows that the strength gained at higher strain rates saturates at the ideal strength of titanium. This occurs at strain rates on the order of $10^6\ s^{-1}$. Frost cautions that the boundaries between the various regions are first approximations, and should not be regarded as exact.

The published reasons for the apparent large increase in strain rate sensitivity at strain rates above $5 \times 10^3\ s^{-1}$ were called into question by Gorham [17–19]. To obtain accurate data from the split-Hopkinson pressure bar [11], certain constraints exist for the specimen geometry and certain assumptions are made concerning the state of stress in the specimen. Gorham presents evidence that these constraints and assumptions were not met, and that the noted increase is due to inertial confinement, specimen dimensions, and a switch away from a one dimensional state of stress. As a result, the argument is made that this transition is not a result of material properties of the specimen, but the test specimen's structure.

In recent review articles Field et al., [20,21] present a summary of high rate testing, and discuss using miniaturized Hopkinson bars to obtain strain rates on the order of $10^5\ s^{-1}$. They also note the increase in strain rate sensitivity at rates $5 \times 10^3\ s^{-1}$ and higher, and concur with Gorham's explanation that it is an artifact of the test configuration. However, they point out that some non-compression tests, where inertia should not be a factor, also show this phenomenon.

In another recent review article by Jia and Ramesh [22], the use of miniaturization of the Split-Hopkinson Pressure Bar to obtain stress–strain behavior at strain rates of up to $5 \times 10^4\ s^{-1}$ is assessed in detail and applied to 6061-T651 aluminum. Due to the small size of the specimens they avoided geometries which would cause errors due to inertia confinement, and demonstrated this by using Gorham's equations [19]. No quasi-static results are presented in this work, however, comparing the presented strain rate sensitivity at strain rates greater than $10^3\ s^{-1}$ with published quasi-static values of this particular alloy appear to show a increase in strain rate sensitivity, but not to the extent shown in Figs. 8 and 9. The authors also state that the explanations of the dramatic increases are occasionally controversial.

Dioh et al., [23] present analytical and numerical evidence which shows that the apparent increase in the strain rate sensitivity reported in the literature may result from stress wave propagation effects present in the test. Oosterkamp et al., [24] tested Aluminum Alloys 6082 and 7108 and found that for these alloys, the sudden change in the strain rate sensitivity is a testing artifact. While Nemat-Nasser et al., [25] show that there is a dramatic increase in strain rate sensitivity at approximately $5 \times 10^3\ s^{-1}$ in a NiTi alloy. They compare images of the failed material at low and high strain rates, demonstrating a different failure mechanism.

In summary, there is disagreement in both the qualitative and quantitative nature of strain rate sensitivity in metals at strain rates greater than approximately $10^5\ s^{-1}$. Some of the published literature definitely states that the increase in slope seen at these

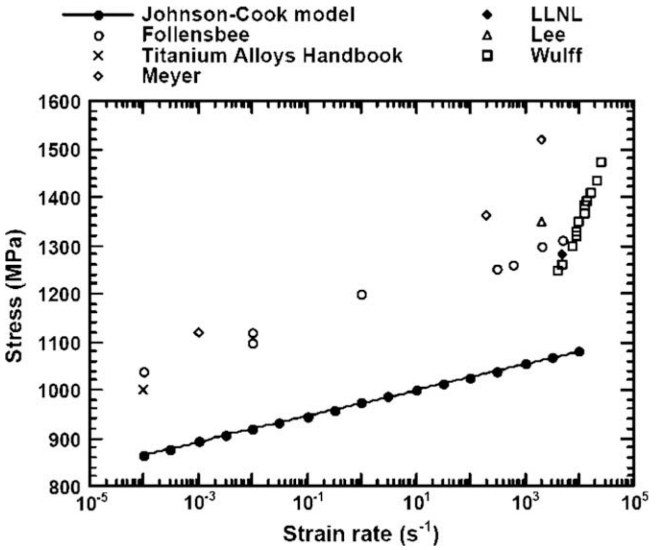

**Fig. 9.** Comparison of the stress–strain rate response of Ti–6Al–4V alloy obtained from this study as well as other studies from the literature. From Ref. [8].

**Table 3**
Ballistic impact test results.

| Test ID | Geometry | Projectile weight | Velocity | Damage description |
|---|---|---|---|---|
| LG456 | Curved | 465.8 gm (1.027 lbs) | 358.4 m/s (1176 ft/s) | *Contained*; small perforations on both slap down corner locations |
| LG455 | Flat | 459.9 gm (1.014 lbs) | 358.4 m/s (1176 ft/s) | *Contained* |
| LG457 | Flat | 463.1 gm (1.021 lbs) | 394.4 m/s (1294 ft/s) | *Contained*; perforation at initial contact location |
| LG458 | Curved | 463.1 gm (1.021 lbs) | 395.3 m/s (1297 ft/s) | *Contained*; perforations on both slap down corner locations |
| LG480 | Flat | 468.1 gm (1.032 lbs) | 423.1 m/s (1388 ft/s) | *Uncontained*; complete projectile size hole with a massive tear running almost the length of the plate |
| LG477 | Flat | 459.9 gm (1.014 lbs) | 426.7 m/s (1400 ft/s) | *Uncontained*; complete projectile size hole |
| LG459 | Curved | 464.0 gm (1.023 lbs) | 430.4 m/s (1412 ft/s) | *Contained*; perforations on both slap down corner locations meet forming single tear |
| LG479 | Flat | 462.2 gm (1.019 lbs) | 457.2 m/s (1500 ft/s) | *Uncontained*; complete projectile size hole with a massive tear running almost the length of the plate |
| LG461 | Curved | 459.9 gm (1.014 lbs) | 460.2 m/s (1510 ft/s) | *Contained*; perforations on both slap down corner locations meet forming single tear |
| LG462 | Curved | 462.2 gm (1.019 lbs) | 490.1 m/s (1608 ft/s) | *Uncontained*; complete projectile size hole with tear beginning on initial contact |

**Fig. 10.** Flat at 394 m/s (1294 fps).

rates is an artifact of testing, while some of the references demonstrate the increase in non-compressive tests where these artifacts would not be present, and some show a change in failure mechanism in microscopic images. It also seems possible that some part of strain rate sensitivity increase seen is a material property and some part a test artifact. Obviously, the effect could also be alloy dependent.

While there is uncertainty to the degree to which the strain rate sensitivity slope increase is caused by material or structural response (testing artifacts), there is significant evidence that there is a change in the response of metals at strain rates of approximately $10^5\ \mathrm{s}^{-1}$ and greater. As discussed in the previous section, the strain rate sensitivity slope increase was included in the analysis as a material property. Including this effect was necessary to match the test results, both threshold velocities and local plastic deflections. Although the inclusion of the strain rate sensitivity increase and the subsequent matching of the test data is suggestive, this does not prove that the increase is a material property. It is also possible that the inclusion of the strain rate sensitivity increase as a material property is somehow compensating for some other phenomena which are not included in the analysis. This possibility will be discussed in Section 4.

**Fig. 11.** Flat at 427 m/s (1400 fps).

**Fig. 12.** Flat at 457 m/s (1500 fps).

## 4. Results and discussion

The results of the ballistic impact tests are shown in Table 3. Photographs of four selected plates and blade projectiles are shown in Figs. 10–14. The blades impacting the curved plates are contained at between 457.2 and 487.68 m/s (1500 and 1600 ft/s) and the blades impacting the flat plates are contained at between 396.24 and 426.72 m/s (1300 and 1400 ft/s). These ballistic test results demonstrate that the radially convex curved containment geometry contains the blade projectile at approximately 60 m/s (200 ft/s) higher than the flat geometry. However, certain conditions must exist for the convex curved surface to be effective. The convex curve case requires sufficient strength and stiffness, relative to the blade, to maintain the curved geometry. Particularly, this includes system stiffness and local strength. System stiffness required to maintain the convex curved shape under impact, would normally be provided by ribs. A simulation of the rib stiffness was required in the test setup to successfully test this concept. The case must also be of sufficient thickness and strength to bend the tips of the incoming blade, without the local section being destroyed.

The plates receive the initial strike from the blade projectile along an edge, which leaves an indentation in the plate. If the velocity of the projectile is high enough, the steel proceeds to tear

**Fig. 13.** Curved at 430 m/s (1412 fps).

**Fig. 14.** Curved at 460 m/s (1510 fps).

catastrophically. At somewhat lower velocities, when the initial edge does not fail, the curved plates experience a perforation when the thick section of blade rotates into the plate, after initial impact. The observed advantage of approximately 60 m/s (200 ft/s), which the radially convex curved plates have over the flat plates, is due to the energy that is absorbed by plastic deformation of the blade tips as they impact the curved surface, and the additional energy absorbed by the plate. The two geometries are compared at 457 m/s (1500 fps) by computing the running total of energy absorbed by the blade as shown in Fig. 16. The energy absorbed by the blade in the curved plate case initially lags the energy absorbed in the flat plate due to its having to travel a slightly farther distance for full contact to be made. Then as the blade travels into the curved section, its tips are bent backward, absorbing energy. Since more of the total energy is absorbed by the blades in the curved geometry, the containment structure is required to absorb less of the total impact energy. As a result, the containment structure may be made lighter or used to absorb higher impact velocities. The running total of energy absorbed by the plate for the same analytical cases is shown in Fig. 17. The energy that the flat and curved plates absorb is nearly identical until general failure occurs in the flat plate.

In explicit finite element analysis, unless localization effects are accounted for, the relationship between effective plastic strain to failure and actual material failure is dependent on the mesh size.

**Fig. 15.** Curved at 490 m/s (1608 fps).

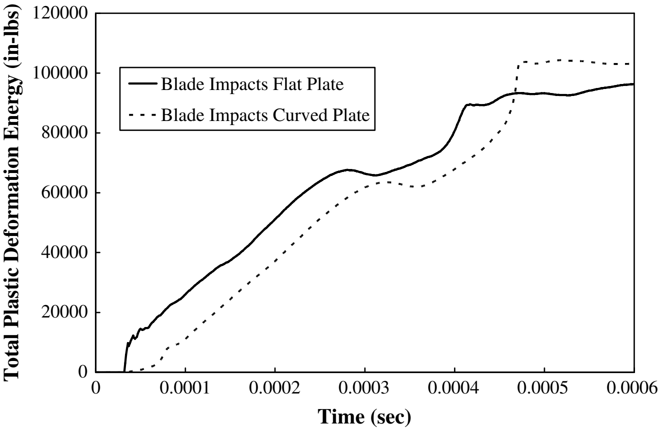

**Fig. 16.** The running total of plastic deformation energy of the blade projectile, comparing the two geometries, at 457 m/s (1500 fps).

Since a non-local failure algorithm has not been used in this analysis, in order to correlate computational models with test results the effective plastic strains to failure, or element erosion, had to be adjusted. The effective plastic strain to failure in this analysis only needed to be adjusted slightly. A sample of this stainless steel was tested statically and found to fail at a plastic strain of 0.352. A value of 0.36 effective plastic strain to failure for the steel was found to reflect the ballistic test results. A value of 0.22 effective plastic strain to failure for the titanium was found to reflect the ballistic test results, which is consistent with published data. The consequence of adjusting the analytical failure strains to match the impact test results is that this particular set of parameters is only appropriate for the particular mesh size. For this set of analysis, once the failure strains were established, the mesh size was not varied.

At the initial contact of the edge of the blade projectile and the plate, extremely high strain rates in both the plate and projectile were calculated by the analysis. Calculated strain rates reached the magnitude of $10^6\ \mathrm{s}^{-1}$ for a short period of time. During that same short time period, stresses in the plate reached a very high level. It was determined that if the dramatic increase in strain rate sensitivity at strain rates greater than $5 \times 10^3\ \mathrm{s}^{-1}$ was not included in the material models, unrealistic premature failure in the plate would inevitably result. If the large increase in strain rate sensitivity was included, as discussed earlier, then the premature, unrealistic failure in the plate was avoided, and a reasonable match between the test and the analysis resulted.

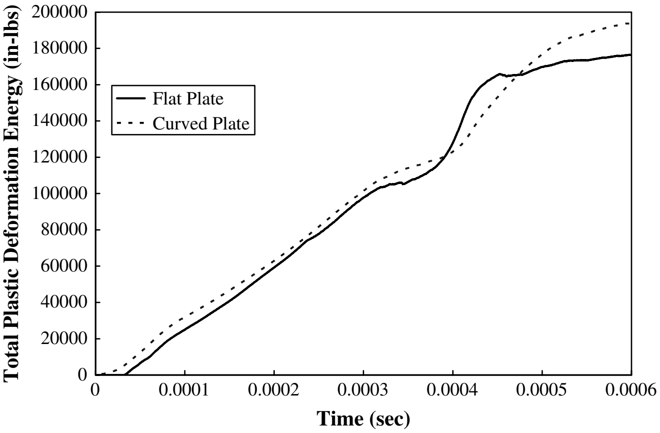

**Fig. 17.** The running total of plastic deformation energy of the plate, comparing the two geometries, at 457 m/s (1500 fps).

**Fig. 18.** Flat analysis 396.2 m/s (1300 ft/s).

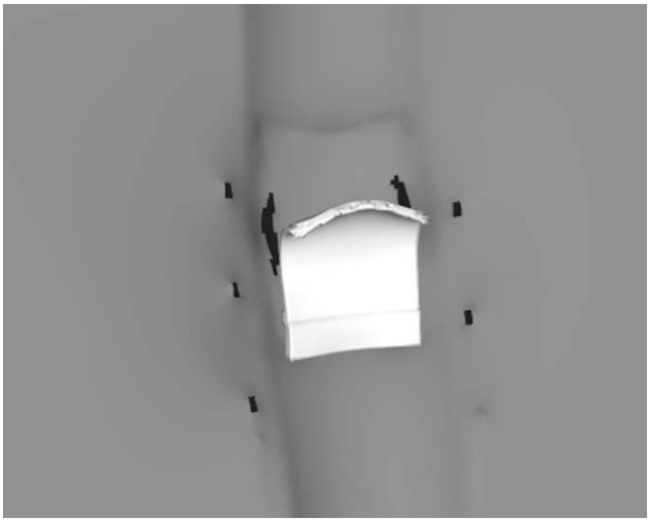

**Fig. 20.** Curved analysis 457.2 m/s (1500 ft/s).

While suggestive, this analysis does not necessarily prove that the dramatic increase in strain rate sensitivity at very high strain rates of many metals, seen in the split-Hopkinson pressure bar tests, is actually a valid material property. There is a possibility that the inertia confinement or stress wave propagation explanations of this behavior are duplicated in the ballistic impact tests, but the shell elements used in the analysis do not model these phenomena. As a result, including the dramatic increase in the material behavior may be compensating for not utilizing a finite element mesh which could represent inertia confinement or stress wave propagation. Increasing the mesh density of the shell mesh is not a solution, as the increasing mesh density leads to greater localization and higher stress values, resulting in even more premature failure. It is possible that a solid element mesh of sufficient density might represent the physics of inertia confinement, stress wave propagation, or some other non-material explanation of the dramatic increase in strain rate sensitivity. However, such a mesh would be impractical for use in a full containment case analysis, and is also beyond the scope the current investigation into the convex curve geometry of that case.

The computational results closely matched the experimental results, especially considering that the exact orientation of the blade upon impact could not be precisely controlled in the test. Images from the analysis matching the conditions of the tests shown in Figs. 10–15 are shown in Figs. 18–21. There were several minor exceptions which should be noted. In the analysis, the blade did not fragment into several pieces at higher velocities, as occurred in the tests. This may be a problem with the simple effective plastic strain to failure in the titanium model, but it could also be due to the great uncertainty in the very high strain rate behavior of the titanium. In addition, the trajectory of the blade, after the initial impact, was somewhat too shallow causing the second impact to occur closer to the initial impact than what was observed in the test. This angle of rebound is almost entirely controlled by the friction value between the plate and the projectile. The exact friction coefficient between the plate and the projectile at these velocities is not known. In the computational analysis point failures occurred at the 0.2032 m (8.0 in) wide simple supports. In the test, the supports were wider and did not produce the stress concentrations to the extent noted in the analysis. Since these point failures were away from the section of interest, and did not lead to catastrophic failure, they were ignored.

The weight saving potential of the convex curved design concept was evaluated by taking the correlated curve plate model, and reducing its thickness until the plate failed. This 396.2 m/s (1300 ft/

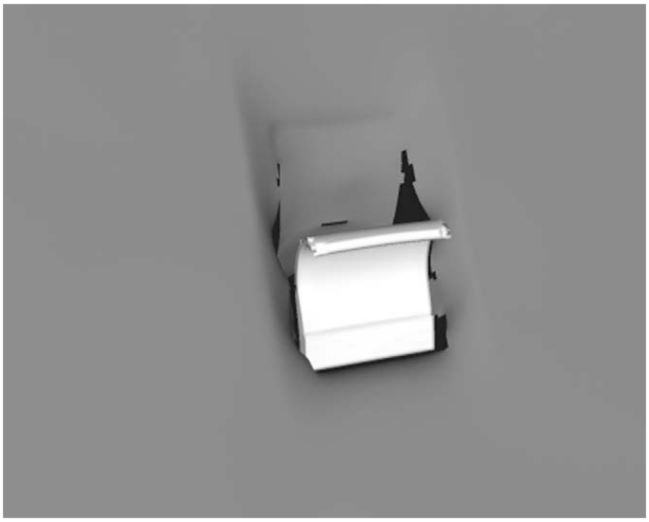

**Fig. 19.** Flat analysis 426.7 m/s (1400 ft/s).

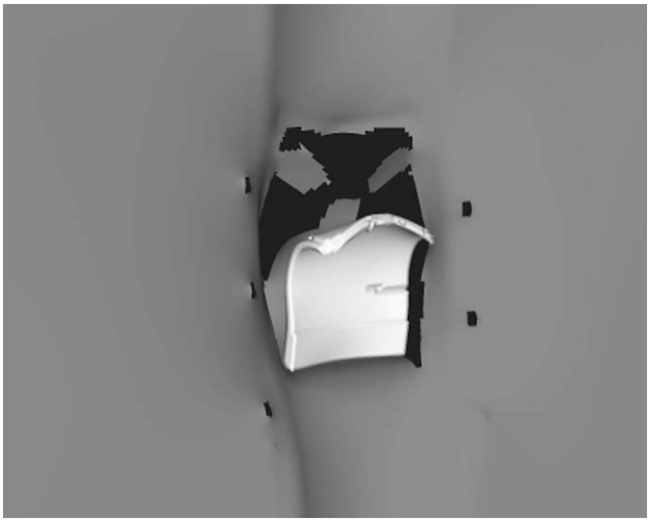

**Fig. 21.** Curved analysis 487.7 m/s (1600 ft/s).

s) velocity impact analysis was compared to the flat plate at the same velocity. The weight of the thinner convex curve section, taking into account its 7.25% greater arc length, was compared to the 0.47625 cm (3/16 in) thick flat plates. It was found that a curved section thickness of 0.381 cm (0.15 in) failed to the same degree as the flat plate baseline, yielding an approximate weight savings of 14% in the curved section of the concatenated fan case. The amount of weight savings that potentially could be realized in a full case would be dependent on the specific actual design, and so is difficult to estimate.

## 5. Conclusion

Using a fan case with a convex curved geometry to increase containment efficiency has been demonstrated both by test and analysis. Both the test results and the correlated analytical model have shown an approximate 60 m/s (200 ft/s) increase in containment capability using the particular curved geometry. Using a curved geometry could in turn lead to a significant weight savings in fan case and engine weight.

A computational model was developed which matches the behavior of the ballistic impact tests. A critical component of the computational model was the material behavior at very high strain rates. The exact nature of the very high strain rate behavior is uncertain, but for high speed impact prediction accuracy, it must be accounted for. Further mechanical property tests to determine the fundamental behavior are warranted.

## References

[1] Federal Aviation Administration. Federal aviation regulation part 33, Section 33.94. 1984.

[2] Carney KS, Lawrence C, Carney DV. Aircraft engine blade-out dynamics. In: Wayne Mindle, editor Seventh international LS-DYNA users conference. Livermore CA, USA: Livermore Software Technology Corporation; 2002. p. 14–17 and 14–26.

[3] Vasko TJ. Fan blade bird-strike analysis and design. In: Wayne Mindle, editor. Sixth international LS-DYNA users conference. Livermore CA, USA: Livermore Software Technology Corporation; 2000. p. 9–13 and 9–8.

[4] Hallquist JO. LS-DYNA keyword user's manual. Livermore, CA: Livermore Software Technology Corp.; 2003.

[5] Hallquist JO, Lin T, Tsay CS. LS-DYNA theoretical manual, nonlinear dynamic analysis of solids in three dimensions. Livermore, CA: Livermore Software Technology Corp.; 1993.

[6] Carney KS, Pereira M, Revilock D, Matheny P. Jet engine fan blade containment using an alternate geometry. In: Fourth European LS-DYNA user's conference. Stuttgart, Germany: DYNAmore GmbH; 2003. p. I-I-01–10.

[7] Nicholas T. Dynamic tensile testing of structural materials using a split Hopkinson bar apparatus. AFWAL-TR-80_4053; 1980.

[8] Lesuer DR. Experimental investigations of material models for Ti–6Al–4V Titanium and 2024-T3 Aluminum. DOT/FAA/AR-00/25; 2000.

[9] Wulf GL. High-strain rate compression of titanium and some titanium alloys. Int J Mech Sci 1979;21:713–8.

[10] Dowling AR, Harding J. In: First International Conference of Center for High-Energy Forming, vol. 2. Denver, CO, USA: University of Denver; 1967. 7.3.1.

[11] Gray GT. High Strain Rate Testing of Materials: the Split-Hopkinson Pressure Bar. LA-UR-97-4419; 1997.

[12] Campbell JD, Ferguson WG. Temperature and rate effects in mild steel. Phil Mag 1970;21:63–82.

[13] Dowling AR, Harding J, Campbell JD. The dynamic punching of metals. J Inst Met 1970;98:215–24.

[14] Campbell JD, Cooper RH. Physical basis of yield and fracture. London: Institute of Physics and Physical Society; 1966. p. 77.

[15] Meyer LW. Strength and ductility of a titanium-Alloy Ti–6Al–4V in tensile and compressive loading under low, medium and high rates of strain. Titanium Sci Technol 1984:1851–8.

[16] Frost HJ, Ashby MF. Deformation-mechanism maps, the plasticity and creep of metals and ceramics. New York: Pergamon Press; 1982.

[17] Gorham DA. The effect of specimen dimensions on high strain rate compression measurements of copper. J Phys D 1991;24:1489–92.

[18] Gorham DA, Pope PH, Field JE. An improved method for compressive stress -strain measurements at very high strain rates. Proc R Soc Lond A 1992; 438:153–70.

[19] Gorham DA. Specimen inertia in high strain rate compression. J Phys Appl Phys 1989;22:1888–93.

[20] Field JE, Walley SM, Proud WG, Goldrein HT, Siviour CR. Review of experimental techniques for high rate deformation and shock studies. Int J Impact Eng 2004;30:725–75.

[21] Field JE, Walley SM, Bourne NK, Huntley JM. Review of experimental techniques for high rate deformation studies. In: Proceedings of the Acoustics and Vibration Asia 98 conference, Singapore; 1998. p. 9–38.

[22] Jia D, Ramesh KT. A rigorous assessment of the benefits of miniaturization in the Kolsky bar system. Exp Mech 2004;44(5).

[23] Dioh NN, Ivankovic A, Leevers PS, Williams JG. Stress wave propagation effects in split Hopkinson pressure bar tests. Proc Math Phys Sci 1936;449:187–204.

[24] Oosterkamp LD, Ivankovic A, Venizelos G. High strain rate properties of selected aluminum alloy. Mater Sci Eng 2000;278:225–35.

[25] Nemat-Nasser S, Choi JY, Guo WG, Isaacs JB. Very high strain-rate response of a NiTi shape-memory alloy. Mech Mater 2005;37:287–98.